In Situ Subwavelength Microscopy of Ultracold Atoms Using Dressed Excited States

R. Veyron, J-B. Gerent, G. Baclet, V. Mancois, P. Bouyer, and S. Bernon*
LP2N, Laboratoire Photonique, Numérique et Nanosciences, Université de Bordeaux-IOGS-CNRS:UMR 5298, rue F. Mitterrand, Talence F-33400, France

(Received 7 December 2023; revised 14 June 2024; accepted 18 July 2024; published 11 September 2024)

In this work, we implement a new method for imaging ultracold atoms with subwavelength resolution capabilities and determine its regime of validity. It uses the laser-driven interaction between excited states to engineer hyperfine ground-state population transfer in a three-level system on scales much smaller than the optical resolution. Subwavelength imaging of a quantum gas is atypical in the sense that the measurement itself perturbs the dynamics of the system. To avoid induced dynamics affecting the measurement, one usually "rapidly" measures the wave function in a so-called strong imaging regime. We experimentally illustrate this regime using a thermal gas ensemble, and demonstrate subwavelength resolution in quantitative agreement with a fully analytical model. Additionally, we show that, counterintuitively, the opposite weak imaging regime can also be exploited to reach subwavelength resolution. As a proof of concept, we demonstrate that this regime is a robust solution to select and spatially resolve a 30-nm-wide wave function, which was created and singled out from a tightly confined one-dimensional optical lattice. Using a general dissipation-included formalism, we derive validity criteria for both regimes. The formalism is applicable to other subwavelength methods.

DOI: 10.1103/PRXQuantum.5.030349

I. INTRODUCTION

Quantum gas microscopes have emerged as essential tools for quantum simulations using cold neutral atoms in optical lattices [1]. For instance, antiferromagnetic long-range order has been measured in standard optical lattices [2,3] by measuring spin correlations between lattice sites with a microscopy that can resolve both atomic density and spin. In this context, subwavelength lattices using, for instance, stroboscopic techniques [4,5], Raman-coupled multilevel states [6], or near-field lattices in front of a surface [7] have emerged as an option to enhance interactions that are essential to enter into strongly correlated phases. Imaging such systems thus requires developing novel techniques to beat the far-field diffraction limit of $\lambda/2$, where λ is the imaging wavelength. The field of bioimaging has long since been confronted with this issue and has developed dedicated methods [8] to bypass this limit like structured illumination microscopy [9], stimulated emission depletion [10], or single-molecule localization [11].

Among the methods applied to cold atoms, some take advantage of a tightly focused beam to image individual sites [12], others use the optical transfer function noise properties and discreteness of the object to gain in resolution [13] or magnify the object using matter-wave optics [14]. We often refer to the works [15,16] that have experimentally pioneered super-resolution imaging of quantum gas. Exploiting the nonlinearity of light-matter interaction, these methods locally transfer atoms from a dark to a bright state and have demonstrated resolutions down to tens of nanometers. In Ref. [15], a strong standing wave of optical pumping light incoherently transfers all atoms except subwavelength slices of atoms that remain in the dark state. In Ref. [16], a two-photon dark state using a standing wave coherently populates the bright state in subwavelength slices. In these methods, the imaging position is determined by the position of the standing waves' minima.

In this work, we both demonstrate and characterize a novel subwavelength imaging method and present a general theoretical formalism based on a Schrödinger equation with dissipation to describe the system dynamics. The formalism allows us to show that subwavelength control can be reached both in the strong and weak imaging limits, which respectively correspond to a diabatic and adiabatic evolution of the system. While only the first has been studied in Refs. [15,16], we show that the second achieves similar performances with reduced timing constraints. The formalism additionally allows us to define

*Contact author: simon.bernon@institutoptique.fr

the validity ranges of the two imaging regimes. The novel demonstrated method relies on an incoherent transfer of subwavelength slices of atoms from a dark to a bright state. The method is based on dressed state engineering that is well adapted to multilevel systems and that has been theoretically investigated for near-field traps [7]: a strong light shift is generated by a spatially varying profile of optical intensity whose radiation frequency is tuned close to an atomic transition between two excited states of ^{87}Rb at 1529 nm. First, in Sec. II, we present the dressing method, modeled by a three-level system, and provide a theoretical formalism that describes the system dynamics during imaging. Validity criteria for the two opposite imaging strength regimes are derived as well as their expected performance. Experimental results are presented in Sec. III. In Sec. III A, we present the main characteristics of the cold-atom apparatus described in more detail in Ref. [17]. Then, in Sec. III B, in the strong imaging regime, we measure the spatial resolution as a function of the light-shift gradient and demonstrate that the resolution can easily be tuned well below the diffraction limit, in good agreement with the model. Finally, in Sec. III C, in the weak imaging regime, we prepare and test the subwavelength resolution on the narrowest atomic density we could prepare via the adiabatic loading of a Bose-Einstein condensate (BEC) in the first band of a tightly confined lattice.

II. METHOD

The method is depicted on Fig. 1. It consists of a spatially dependent incoherent transfer of atomic populations between the hyperfine ground states $|1\rangle$ and $|2\rangle$ via their common coupling to a dressed excited state $|2'\rangle$. The energy of $|2'\rangle$ is spatially modulated such that a homogeneous repumper excitation is only locally resonant and the population transfer occurs on scales that are not limited by diffraction. After removing the dressing field, the population transferred in $|2\rangle$ is imaged on a cycling transition from $|2\rangle$ to $|3'\rangle$.

Experimentally, as shown in Fig. 1(a), a 1529-nm laser lattice intensity profile drives the transition between the two excited states $5^2P_{3/2}$ and $4^2D_{5/2}$ of ^{87}Rb, resulting in a spatially dependent light shift for the excited state $|2'\rangle$ [Fig. 1(b)]. The excited-state potential is therefore given by

$$U_{5P}(x) = U_{5P,0}\cos^2\left(\frac{k_{1529}}{2}x - \frac{\pi}{4}\right), \tag{1}$$

where $k_{1529} = 2\pi/i_{1529}$ is the lattice wave vector, i_{1529} is the lattice period, and $U_{5P,0}$ is the total amplitude that is given by the maximum of the 1529-nm laser intensity profile I_{1529}. This amplitude is computed from the diagonalization of the standard electric dipole and hyperfine Hamiltonians, as detailed in Appendix A. We restrict our model to the linear light-shift regime where the amplitude is proportional to the intensity.

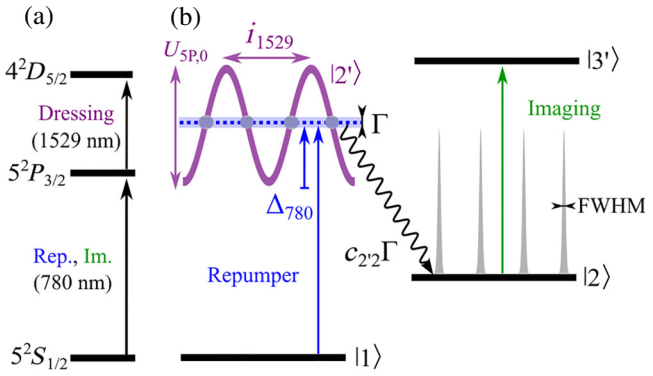

FIG. 1. (a) Three fine structure states of ^{87}Rb: the ground state $5^2S_{1/2}$ and the two excited states $5^2P_{3/2}$ and $4^2D_{5/2}$. (b) A three-level system with an optically dressed excited state using a 1529-nm lattice probed with a repumper at a detuning Δ_{780} and imaged on a cycling transition.

The spatially dependent detuning of the 780-nm laser with respect to the bare hyperfine states is

$$\Delta(x) = \Delta_{780} - \Delta_{LS}(x), \tag{2}$$

where $\Delta_{780} = \omega_{780} - \omega_0$ is the bare detuning between the laser frequency ω_{780} and the bare atomic transition frequency ω_0, $\Delta_{LS}(x) = U_{5P}(x) - U_{5S}(x)$ is the differential light shift between the ground and excited states, and $U_{5S}(x)$ is the potential of the ground state that is small compared to the excited-state light shift. In the low-saturation limit ($s_0 \ll 1$), the spatially dependent saturation parameter is given by

$$s(x) = \frac{s_0}{1 + [2\Delta(x)/\Gamma]^2} \approx \frac{s_0}{1 + (x/X_0)^2}, \tag{3}$$

where $\Gamma/2\pi = 6.066$ MHz and $s_0 = I_{780}/I_{sat,rep}$ are respectively the natural linewidth and the on-resonance saturation parameter for the repumper transition, with I_{780} the intensity of the repumper beam and $I_{sat,rep}$ the saturation intensity of the optical transition. The last expression in Eq. (3) will be used in the rest of the manuscript. It corresponds to a repumper laser tuned at the middle of the excited-state modulation such that $\Delta_{780} = U_{5P,0}/2$, where the spatial selectivity of the method is maximal. Around $x = 0$ the detuning can be linearized [$\Delta(x) = \pi U_{5P,0}x/i_{1529}$] and a transfer occurs on a scale given by the localization length

$$X_0 = \frac{i_{1529}\Gamma}{2\pi U_{5P,0}}. \tag{4}$$

We now focus on deriving the point spread function of this subwavelength imaging method. In ultracold atomic physics the particles' wave functions are larger than

achievable subwavelength resolutions, which is a different regime than encountered in bioimaging. Such localized modification of the wave function leads to a spatiotemporal dynamics of the wave function during the imaging process that one needs to account for. To simplify the study, Refs. [15,16] have tried to decouple the spatial and temporal dynamics using the strong imaging regime that they reached via a rapid transfer. We derive below the validity criteria of such a regime and show that rapidity is not the sole criteria to reach subwavelength imaging.

Temporal transfer dynamics. In Appendix B, we give the multilevel structure of ^{87}Rb and justify the choice of a three-level system (3LS) model to describe the population transfer from $|1\rangle$ to $|2\rangle$. As detailed in Appendix C 1 and in Ref. [15], for all parameters used in this work, the transfer rate of the population at position x is independent of time and can be very well approximated by

$$\kappa(x) = \frac{c_{2'2}\Gamma}{2} s(x) \approx \frac{\kappa_0}{1 + (x/X_0)^2}, \tag{5}$$

where the on-resonance transfer rate is $\kappa_0 = c_{2'2}\Gamma s_0/2$. Equation (5) leads to an exponential growth of the population in $|2\rangle$ with a rate proportional to the branching ratio ($c_{2'2}$) between $|2'\rangle$ and $|2\rangle$ and the scattering rate at position x.

Spatiotemporal dynamics. In the following, we only consider the spatial dynamics of $|1\rangle$. Indeed, once atoms have been transferred to $|2\rangle$, their spatial evolution will not impact the imaging resolution that is only sensitive to the number of transferred particles. Following previous works [18–20], the effect of the transfer rate $\kappa(\hat{x})$ on the evolution of the wave function $\Psi(x,t)$ for atoms in $|1\rangle$ can be accounted for by a loss term in the Schrödinger equation

$$i\hbar \frac{d|\Psi(x,t)\rangle}{dt} = \hat{H}_0 |\Psi(x,t)\rangle - i\frac{\hbar\kappa(\hat{x})}{2} |\Psi(x,t)\rangle \tag{6}$$

where $\hat{H}_0$ is the Hamiltonian including kinetic and potential energies of a harmonic oscillator, and $\kappa(\hat{x})$ is a rate operator derived from Eq. (5). The Hamiltonian $\hat{H}_0$ satisfies $\hat{H}_0 |\phi_n\rangle = E_n |\phi_n\rangle$, where the $|\phi_n\rangle$ are eigenstates, and the $E_n = \hbar\omega_{\mathrm{HO}}(n + 1/2)$ are the eigenvalues with ω_{HO} the harmonic oscillator trap frequency.

This formalism allows us to define the strong and weak imaging regimes.

(a) Strong imaging: a high transfer rate κ_0 is used during a very short imaging time. The wave function is strongly affected, but has no time to evolve before the end of the transfer.
(b) Weak imaging: a weak transfer rate κ_0 is applied during a long imaging time, allowing the wave function to remain in the ground state throughout the process.

Their applicability domain is presented below and we show that both are relevant to perform subwavelength imaging.

A. Strong imaging regime

As discussed in Refs. [15,16], a rapid transfer can be used to super-resolve a wave function. This process creates a dip of width Δx in the initial wave function that corresponds to a velocity spread Δv that is minimal for a Gaussian spatial localization. In this case, we achieve equality of the Heisenberg uncertainty principle: $\Delta v \Delta x = \hbar/(2m)$ with m the mass of the particle. The strong imaging regime ($t_{\mathrm{tr}}\Delta v \ll \Delta x$) is then fulfilled for transfer time

$$t_{\mathrm{tr}} \ll 2m\Delta x^2/\hbar. \tag{7}$$

For a 10-nm Gaussian standard deviation localization of ^{87}Rb atoms, this amounts to 273 ns and is more restrictive for non-Gaussian localization.

The quite general case of a Lorentzian transfer rate of full width at half maximum $\mathrm{FWHM_s}$, achieved here with optical pumping [Eq. (5)], leads to a velocity spread Δv derived in Appendix C 3. In the strong imaging regime, the imaging time should satisfy $t_{\mathrm{tr}}\Delta v \ll \mathrm{FWHM_s}$, which yields the following condition on the transfer rate:

$$\mathcal{S} = \frac{2}{\ln(2)} \frac{\hbar\kappa_0}{\hbar^2/(2mX_0^2)} \gg 1. \tag{8}$$

Here we have shaped the equation to emphasize the energy ratio of pumping strength $\hbar\kappa_0$ over localization recoil $\hbar^2/(2mX_0^2)$. One should note that this criterion does not restrict the imaging time, but rather constrains the imaging strength κ_0, and hence the name "strong," rather than "fast," imaging regime.

The strong imaging regime is experimentally demonstrated in Sec. III B below. The atomic density in $|2\rangle$ at position x and time t for a repumper resonant at position x_r is

$$\rho_{22}^s(x, x_r, t) = \rho_{00}(x, t = 0)(1 - e^{-\kappa(x - x_r)t}), \tag{9}$$

where $\rho_{00}(x, t = 0)$ is the initial atomic density for atoms in $|1\rangle$. For a homogeneous initial density [$\rho_{00}(x, t = 0)$ constant], the width of ρ_{22} as a function of x is the characteristic scale of the super-resolution imaging.

For a long pulse duration compared to the internal state dynamic ($s_0\Gamma t_{\mathrm{tr}} \gg 1$) and for well-resolved fringes such that $\Gamma/U_{5\mathrm{P},0} \ll 1$, we can compute the full width at half maximum of Eq. (9) at the middle of the modulation where $\Delta_{780} = U_{5\mathrm{P},0}/2$:

$$\mathrm{FWHM_s} = 2X_0\sqrt{\frac{\kappa_0 t_{\mathrm{tr}}}{\ln(2)}}. \tag{10}$$

As detailed in Sec. III B below, for our experimental implementation, Eq. (10) yields spatial widths smaller than the diffraction limit ($\lambda/2 = 390$ nm).

B. Weak imaging regime

In the weak imaging regime, the perturbation introduced by imaging occurs at a slow rate κ, preventing the transfer of population to any excited state of motion. In other words, this regime is achieved when the evolution of the wave function in the internal state $|1\rangle$ is adiabatic with respect to any of the nth vibrational levels of the harmonic oscillator $|\phi_n\rangle$ [21]:

$$\left|\langle\phi_n|\frac{d}{dt}|\Psi(x,t)\rangle\right| = \left|\langle\phi_n|\frac{\kappa(\hat{x})}{2}|\phi_0\rangle\right| \ll \frac{E_n - E_0}{\hbar}. \tag{11}$$

The equality in Eq. (11) is obtained using Eq. (6), the harmonic oscillator modes' orthogonality, and a state initially prepared in the ground state $|\Psi(x,0)\rangle = |\phi_0\rangle$ with harmonic oscillator width $a_{\mathrm{HO}} = \sqrt{\hbar/(m\omega_{\mathrm{HO}})}$. This condition is analytically derived in Appendix C 4, and, for $r_0 \ll 1$, simplifies to

$$\begin{aligned}\mathcal{W}_2 &= \sqrt{\frac{\pi}{8}}\frac{r_0\kappa_0}{2\omega_{\mathrm{HO}}} \ll 1,\\ \mathcal{W}_1 &= \sqrt{\pi}e^{-\frac{1}{2}}\frac{r_0\kappa_0}{2\omega_{\mathrm{HO}}} \ll 1,\end{aligned} \tag{12}$$

where $r_0 = X_0/a_{\mathrm{HO}}$ is the ratio of the localization length over the wave-function width. Therefore, $r_0 \ll 1$ corresponds to resolving the wave-function details. Criteria $\mathcal{W}_2$ and $\mathcal{W}_1$ are the adiabaticity criteria for centered and off-centered coupling terms, respectively. We emphasize once more that this regime depends on the imaging strength κ_0 and not on the transfer time t_{tr}.

In this regime, the number of atoms $\rho_{22}(x_r, t)$ transferred to $|2\rangle$ at time t for a resonant repumper position x_r is given by

$$\begin{aligned}\rho_{22}^{w}(x_r,t) &= N_0(1 - e^{-\langle\phi_0|\kappa(\hat{x}-x_r)|\phi_0\rangle t})\\ &\approx N_0\,\langle\phi_0|\,\kappa(\hat{x}-x_r)\,|\phi_0\rangle\,t,\end{aligned} \tag{13}$$

where N_0 is the atom number in state $|1\rangle$ in the ground state of the harmonic oscillator.

The rate is maximum for $x_r = 0$: $\langle\phi_0|\,\kappa(\hat{x})\,|\phi_0\rangle = \sqrt{\pi}r_0e^{r_0^2}\mathrm{erfc}(r_0)\kappa_0$. The approximated linearized expression in Eq. (13) is satisfied in the limit of weak depletion [$\langle\phi_0|\,\kappa(\hat{x})\,|\phi_0\rangle\,t_{\mathrm{tr}} \ll 1$]. Here $\langle\phi_0|\,\kappa(\hat{x}-x_r)\,|\phi_0\rangle$ corresponds to the Voigt function whose size is given within a 1.2% error by [22]

$$\begin{aligned}\mathrm{FWHM_w^{total}} &= X_0 + \sqrt{X_0^2 + 4a_{\mathrm{HO}}^2\ln(2)}\\ &\approx 2a_{\mathrm{HO}}\sqrt{\ln(2)} + \left(1 + \frac{r_0}{\sqrt{\ln(2)}}\right)X_0.\end{aligned} \tag{14}$$

Equation (14) gives the typical width of the measured density profile, which is the initial harmonic oscillator width broadened by the imaging resolution length X_0.

We note that the validity criteria of weak imaging upper bounds the scattering rate by the harmonic oscillator frequency. This partly reduces the capability of the weak regime to measure fast enough to capture the oscillation dynamics in the lattice. A possible solution to reduce the imaging timescale is to use a large atomic ensemble $N_0 \gg 1$. In that case, even at small t_{tr}, some atoms get transferred by a statistical process. Nevertheless, for short timescale imaging, the strong imaging regime is certainly to favor.

III. RESULTS

The experimental setup used to produce and image the atomic clouds is presented in Sec. III A. Atom numbers are precisely measured using a calibrated *in situ* absorption imaging [17]. The next two parts are demonstrations of the strong and weak imaging regimes. In Sec. III B (strong imaging), we consider the case of a cigar-shaped thermal atomic cloud and a 1529-nm lattice that can be resolved by our imaging system. To validate our model, we measure the number of atoms transferred into state $|2\rangle$ and compare it to the expected atom number deduced from our model. Finally, in Sec. III C (weak imaging) we use the method to prepare and test the subwavelength resolution on the narrowest atomic density we could prepare via the adiabatic loading of a Bose-Einstein condensate in the first band of a tightly confined one-dimensional (1D) lattice with a spacing smaller than the diffraction limit.

A. Absolute calibration of the scattering cross section

We prepare an atomic cloud of ^{87}Rb in state $|1\rangle$ using a hybrid trap composed of a magnetic trap compensating the gravity field and a crossed dipole trap (DT1 and DT2) [23]. Evaporative cooling is performed to produce either a thermal cloud or a BEC.

As shown in Figs. 2 and 4 below, the 1529-nm lattice intensity is generated by the interferences of co- or counterpropagating laser beams with a linear polarization aligned along z that is set as the quantization axis. A π-polarized repumper pulse transfers the atoms to state $|2\rangle$ that is imaged using a cycling transition. The saturation parameters of the repumper and imaging beams are computed for each experimental run by monitoring their optical power.

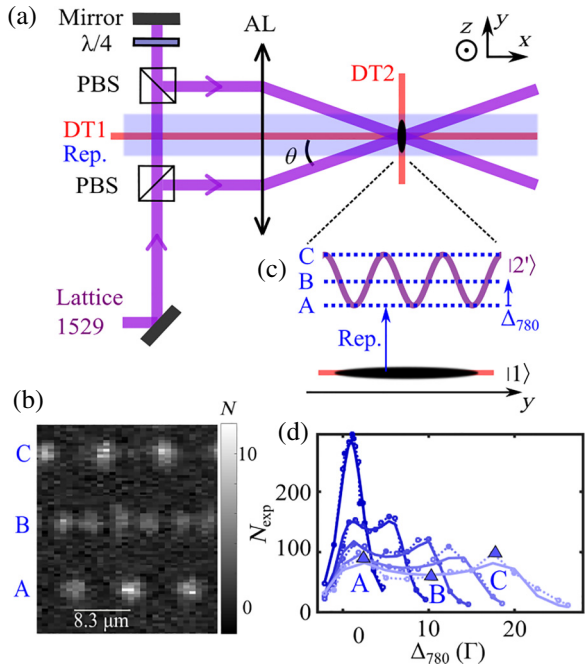

FIG. 2. (a) Optical setup for the generation of the 1529-nm lattice using a combination of mirrors, polarizing beam splitters (PBSs), a quarter-wave plate ($\lambda/4$), and an aspherical lens (AL). (b) Two-dimensional absorption images of repumped atom numbers per pixel for a homogeneous atomic cloud. The letters A, B, and C correspond to the bottom, middle, and top of the lattice, as shown in (c), showing the different resonance conditions between the dressed excited state $|2'\rangle$ and the ground state $|1\rangle$. (d) Integrated atom number per lattice period (dashed lines with circles) for depths $U_{5P,0}$ of 2.5Γ (dark blue), 7.2Γ, 11.6Γ, 15.8Γ, and 21Γ (light blue), and fits (solid lines) with Eq. (15) where the free parameters are the light shift and the total atom number. The light blue curve (21Γ) corresponds to the data of panel (b).

We use a high numerical aperture absorption imaging system with a resolution limit of 1.3 μm [24]. An image with atoms I_{at}, a reference image I_{noat} of the imaging beam, and an image for the background I_{back} are acquired to compute the transmission $T = (I_{at} - I_{back})/(I_{noat} - I_{back})$ and the optical density (OD) given by $b = -\alpha \ln(T) + s_{im}(1 - T)$, where the saturation parameter for the imaging beam is set at $s_{im} = 1$ for a duration of 8 μs.

For accurate atom number measurements, it has been crucial to calibrate the reduction factor α of the scattering cross section that scales linearly with the optical density [17,25]. In Ref. [17], we measured $\alpha(b) = \alpha_0 + \beta b$, where $\alpha_0 = 1.17$ and $\beta = 0.255$. Using this correction, the optical density is reformulated as $b = [-\alpha_0 \ln(T) + s_{im}(1 - T)]/[1 + \beta \ln(T)]$. Finally, the experimental atom number $N_{at} = \iint b(x,y)dxdy/\sigma_0$ can be computed for any region of the image and uses the scattering cross section of a σ^--polarized probe ($\sigma_0 = 2.907 \times 10^{-9}$ cm^2).

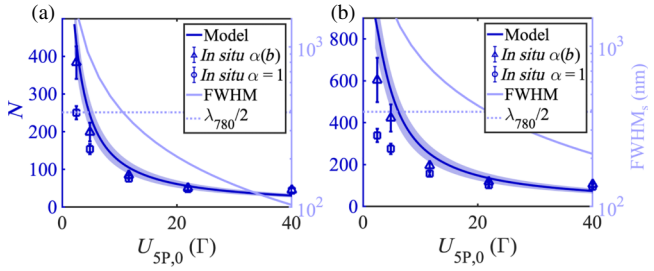

FIG. 3. Atom number (left axis) per unit of lattice period as a function of the light shift on the excited state $|2'\rangle$ when $\Delta_{780} = U_{5P,0}/2$. The expected atom number is computed from the 3LS model with time-of-flight measurements (solid line), or *in situ* with $\alpha = 1$ (circles) and $\alpha = \alpha(b)$ (triangles). The FWHM (right axis) corresponds to the full width at half maximum given by Eq. (10). The diffraction limit is shown by the dotted line. The 780-nm laser parameters are (a) $s_0 = 0.022$, $t = 8$ μs and (b) $s_0 = 0.063$, $t = 12$ μs.

B. Strong imaging regime with thermal atoms

For this experiment, we prepare and characterize by time of flight an initial thermal cloud containing $N_{at}^{tot} = 1.03(16) \times 10^5$ atoms in $|1\rangle$ at a temperature of 169(10) nK, just above the condensation threshold. The cloud is trapped and compressed solely in DT2, creating a cigar-shape elongated along y. The atomic density is then homogeneous over a few 1529-fringe periods ($i_{1529} = 8.3$ μm). A homogeneous magnetic bias of 280 mG along z defines the quantization axis. The maximum density at the cloud center is 1.8×10^{19} at/m^3, giving an optical density of 31. To avoid high OD distortion of atom number counting, we reduce the OD using coherent microwave (MW) transfer between states $|1\rangle$ and $|2\rangle$ with transfer probability function $P(t_{MW}) = P_m \sin^2(\pi t_{MW}/T_{MW})$, where $T_{MW} = 56$ μs is the period and $P_m = 0.96$ is the maximum probability. A first MW π pulse transfers all atoms from $|1\rangle$ to $|2\rangle$ and is followed by a short optical repumper pulse that empties the ground state $|1\rangle$. A second MW pulse of duration $t_{MW} = 8$ μs is used to transfer a controlled population back into $|1\rangle$ and a resonant $|2\rangle$ to $|3'\rangle$ laser pulse pushes away the remaining atoms in $|2\rangle$. This sequence reduces the maximum optical density down to 6. In this configuration, the measured *in situ* cloud widths are $\sigma_y = 64$ μm and $\sigma_x = 2.4$ μm. The subwavelength imaging method described in Sec. II A is then performed on this thermal sample. The use of the wave-function model is justified as the de Broglie wavelength ($\lambda_{dB} = 460$ nm) is higher than the localization length ($X_0 = 33$ nm for $U_{5P,0} = 40\Gamma$). This also allows us to neglect the residual thermal energy contribution to the spatiotemporal dynamics in Eq. (6).

In the copropagating case depicted in Fig. 2(a), the lattice period is $i_{1529} = 8.3$ μm. At midfringe, the clouds are separated by 4.15 μm, which is well resolved by our microscope objective. This allows us to measure the

number of transferred atoms N_{exp} that is obtained by integrating the atomic density over one fringe. We additionally compute theoretically the expected atom number N_{th} without any adjustable parameter by integrating the repumped fraction $\rho^s_{22}(y, y_r, t_{\mathrm{im}})$ of the strong imaging regime [Eq. (9)] over a width of one lattice period:

$$N_{\mathrm{th}}(y_r) = \frac{P(t_{\mathrm{MW}})N^{\mathrm{tot}}_{\mathrm{at}}}{\sqrt{2\pi}\sigma_y}\int_0^{i_{1529}} \rho^s_{22}(y, y_r, t_{\mathrm{im}})dy. \qquad (15)$$

Figure 2(b) shows *in situ* images of the atom number per pixel for three values of the repumper detuning ($\Delta_{780} = 0, U_{5\mathrm{P},0}/2, U_{5\mathrm{P},0}$) for an excited-state light shift of $U_{5\mathrm{P},0} = 21\Gamma$. Given that the 1529-nm lattice period is spatially resolved when the detuning is scanned, these images correspond to a tomography of the excited state. Figure 2(d) shows the number of transferred atoms N_{exp} as a function of the repumper frequency for various excited-state light shifts. Points A, B, C respectively correspond to the bottom, middle, and top of the 1529-nm lattice, as shown in Fig. 2(c). The width from point A to point C is a measure of the light shift and exactly matches with theoretical computations (see Appendix A). Knowing the light shifts and the repumper saturation, $\mathrm{FWHM_s}$ [Eq. (10)] and N_{th} [Eq. (15)] can be straightforwardly computed. An uncertainty of 15% on N_{th} originates mainly from the uncertainty on the determination of the total number of atoms $N^{\mathrm{tot}}_{\mathrm{th}}$.

Figure 3 shows the expected atom number N_{th} and the experimental number N_{exp} as a function of the light-shift amplitude $U_{5\mathrm{P},0}$ for two repumper saturations. The saturation and duration of the repumper have been chosen such that the number of scattered photons on the repumper transition varies from 1 to 10 with either $s_0 = 0.022$ with $t = 8\,\mu\mathrm{s}$ or $s_0 = 0.063$ with $t = 12\,\mu\mathrm{s}$. For the smallest saturation $s_0 = 0.022$, the validity criterion in strong imaging $\mathcal{S}$ is higher than 1. It ranges from 460 ($U_{5\mathrm{P},0} = 2.5\Gamma$) to 1.8 ($U_{5\mathrm{P},0} = 40\Gamma$). For larger saturations, the adiabaticity is more easily fulfilled. In Appendix C 5, we checked that the strong imaging regime applies by numerically solving the Schrödinger equation (6).

In Fig. 3, we see that using the correct atomic scattering cross section $[\sigma_0/\alpha(b)]$ leads to very good agreement between the experimental and theoretical atom numbers $N_{\mathrm{exp}}[\alpha(b)] \approx N_{\mathrm{th}}$. In comparison, we show the case of uncorrected data ($\alpha = 1$) and we see that $N_{\mathrm{exp}}(\alpha = 1) < N_{\mathrm{th}}$ in the low light-shift limit that is where the transferred population $|2\rangle$ is the largest and the multiple scattering effects are the strongest [17]. For large light shifts ($U_{5\mathrm{P},0} = 40\Gamma$), we detect more atoms than the model predicts. We attribute this discrepancy to the coupling of the repumper to other hyperfine excited states and to state mixing effects that are not included in the 3LS model.

The agreement in the experimental and theoretical atom numbers confirms the validity of our model. As a result, we show the associated spatial resolutions given by Eq. (10) on the right axes in Fig. 3. For a large lattice spacing of 8.3 μm, we reached an FWHM of the repumped fraction of 100 nm, which is smaller than the diffraction limit of $\lambda/2 = 390$ nm. This resolution being inversely proportional to the lattice spacing, it is expected to gain a factor $8.3/0.77 = 10.8$ by using counterpropagating beams.

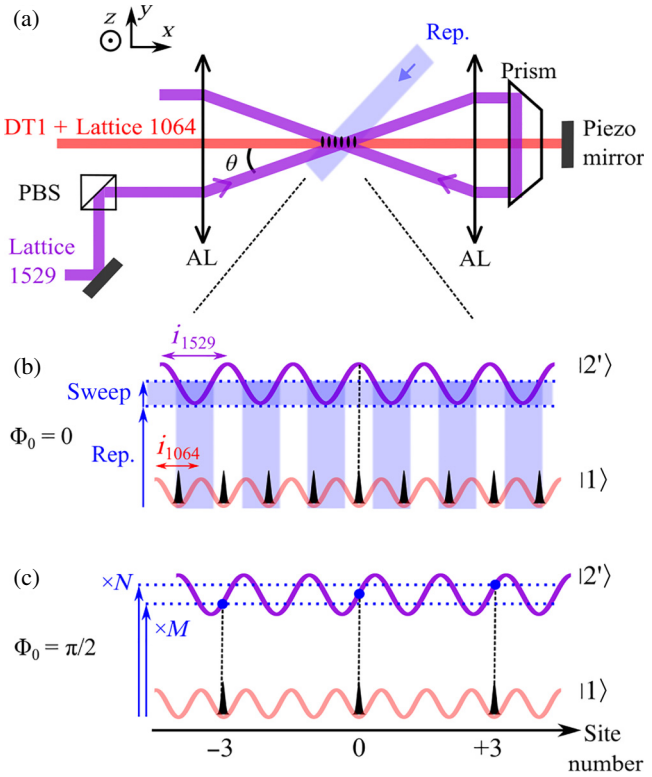

FIG. 4. (a) Optical setup for the generation of the 1529- and 1064-nm lattices. (b) The two lattices with a relative phase $\Phi_0 = 0$. The blue shaded area corresponds to a sweep of the repumper frequency during the coarse cleaning of the lattice. (c) The two lattices with a relative phase $\Phi_0 = \pi/2$. Here M (respectively N) corresponds to the number of repumper pulses at a specific frequency for the fine cleaning of the -3 (respectively $+3$) sites.

C. Weak imaging regime with a tightly confined lattice

We now apply our method to image the longitudinal atomic density of a 1D optical lattice. For that purpose, the atoms are evaporated in a hybrid trap with the single dipole beam DT1 to reach the Bose-Einstein condensation with 2×10^5 atoms. After compression of DT1, the trap frequencies are (15, 160, 160) Hz along (x, y, z). The atoms are then loaded in a 1064-nm lattice that is adiabatically ramped up from 0 to $40E_r$, where $E_r = \hbar^2 k^2_{1064}/(2m)$ is the recoil energy at 1064 nm. The lattice depth $U_{5\mathrm{S},0}$ has been characterized at the atom position using Kapitza-Dirac scattering [26,27]. The lattice is compressed up to $1000E_r$ after removing the magnetic gradient and defining the quantization axis via an homogeneous magnetic bias

of 280 mG along z. The width of the ground-state wave function is given by the harmonic oscillator width $a_{\mathrm{HO}} = \sqrt{\hbar/(m\omega_{\mathrm{HO}})}$, where $\omega_{\mathrm{HO}} = 2\sqrt{U_{5\mathrm{S},0}E_r}/\hbar$ is the trap frequency of one site. The standard deviation (SD) of the atomic density along x is therefore expected to be equal to $\sigma_x = a_{\mathrm{HO}}/\sqrt{2} = 21.2$ nm. Along the y direction, we experimentally measured a width $\sigma_y = 6$ μm. Because the potential is rotationally symmetric about x, we can assume that $\sigma_z = \sigma_y$.

The ground-state lattice with a period of $i_{1064} = \lambda_{1064}/2 = 532.23$ nm is formed by two counterpropagating beams [see Fig. 4(a)], yielding a ground-state trapping potential given by

$$U_{5\mathrm{S}}(x) = U_{5\mathrm{S},0}\cos^2\left(\frac{k_{1064}}{2}x + \frac{\Phi_0}{2}\right), \tag{16}$$

where $k_{1064} = 2\pi/i_{1064}$ is the lattice wave vector and Φ_0 is the relative phase between the 1529- and 1064-nm lattices. As shown in Figs. 4(b) and 4(c), if $\Phi_0 = 0$ then both lattice extrema coincide for a central site, while if $\Phi_0 = \pi/2$, the same central site is aligned at the midfringe of the 1529-nm lattice. The relative phase between the two lattices is controlled by a piezo stack that moves the reflecting mirror of the 1064-nm lattice (see Appendix E).

The 1529-nm lattice is generated along the 1064-nm lattice by reflecting a 1529-nm beam with a prism with an angle θ such that the lattice period is $i_{1529} = \lambda_{1529}/[2\cos(\theta)]$. Because of the different 1064- and 1529-nm lattice periodicities, a perfect commensurability is obtained for a given number of sites n_{1064} at 1064 nm for the ground state and n_{1529} at 1529 nm for the excited state such that

$$n_{1529}i_{1529} = n_{1064}i_{1064}. \tag{17}$$

This gives sets of angles for θ for which the commensurability is obtained:

$$\theta = \mathrm{acos}\left(\frac{n_{1529}\lambda_{1529}}{n_{1064}\lambda_{1064}}\right). \tag{18}$$

Because of experimental mechanical constraints, the only accessible angle in our setup is $\theta = 5.92°$, for which we have $n_{1064} = 13$ and $n_{1529} = 9$. We therefore have a superlattice period of 6.9 μm, where every 13 periods of the 1064-nm lattice, the atoms will see exactly the same modulation of the 1529-nm lattice in the excited state. This superlattice period is large and can be resolved easily by our microscope objective that enables the super-resolution of the lattice sites.

To demonstrate the performances of the method, we now aim at measuring the standard deviation of a single site that we label site number 0. We start by preparing that single site in two steps. In a first step, we perform a coarse cleaning stage in which all sites except sites 0 and ±3, as indexed in Fig. 4(b), are repumped. For that purpose, we spatially shift the excited state using a 1529-nm modulation of $U_{5\mathrm{P},0} = 17\Gamma$ and repump the atoms, while sweeping in 10 ms the detuning of the repumper from $\Delta_{780} = 0.4U_{5\mathrm{P},0}$ to $U_{5\mathrm{P},0}$ at a saturation of $s_0 = 2\times10^{-3}$. All repumped atoms are then pushed away with a resonant $|2\rangle$ to $|3'\rangle$ push laser pulse. In a second step, the piezo is ramped in 100 ms by a distance of $i_{1529}/4$ to align site 0 onto a slope of the 1529-nm modulation, as shown in Fig. 4(c). Sites +3 (respectively −3) are cleaned using N (respectively M) short repumper pulses at $\Delta_{780} = 3\Gamma$ (respectively $\Delta_{780} = U_{5\mathrm{P},0} - 3\Gamma$). Finally, the atomic density is imaged by varying the relative phase Φ_0 and applying a last repumper pulse of detuning $\Delta_{780} = U_{5\mathrm{P},0}/2$, saturation $s_0 = 0.02$, and duration $t = 16$ μs. Such parameters correspond to a weak imaging validity criterion. Indeed, using $r_0 = 0.24$, $\mathcal{W}_2, \mathcal{W}_1 = 0.02, 0.03$, which are indeed small compared to 1. In Appendix C 5, we verify that the weak imaging regime applies by numerically solving the Schrödinger equation (6). Such simulation does not account for the doubly dressed state contribution to the potential [7] that is shown, in Appendix D, to have a negligible effect for the considered experimental realization. The corresponding atomic densities are shown in Figs. 5(a)–5(c). Each curve is fitted by a Gaussian function from which the central position and SD are shown in Figs. 5(d) and 5(e).

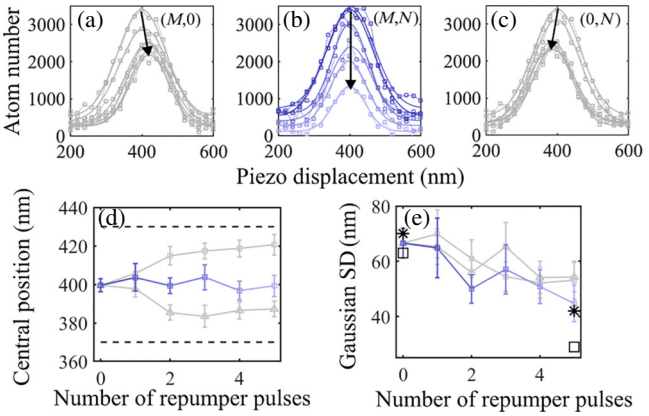

FIG. 5. (a)–(c) Wavepacket density imaging by scanning the piezo mirror. The arrows indicate an increasing number of cleaning pulses of respectively $(M,0)$, $(M,N=M)$, and $(0,N)$, where M and N vary from 0 to 5 pulses. Dotted lines with squares are the data and the lines are Gaussian fits from which the central position (d) and width (e) are extracted. Error bars are fit errors. In (e), the two squares (respectively stars) show the theoretical widths for $\eta_y = 0°$ (respectively $\eta_y = 0.3°$).

As M increases while $N = 0$ [Fig. 5(a)], cleaning only sites −3 shifts the wavepacket to the right, after which it remains stable. In that case we can consider that the −3 site is empty. As site 0 is centered at the middle of

the excited-state modulation, sites ± 3 would be resonant exactly at $(3i_{1064} - 2i_{1529}) = 60$ nm away from that central position. Therefore, for equal initial populations in sites $-3, +3, 0$, the central position should shift by at maximum 30 nm. However, during the coarse cleaning stage, the ± 3 sites are closer from resonance than site 0 and the repumper therefore induces more scattering on these sites and reduces more their population. These unequal populations would lead to a smaller shift of the central position. From numerical simulations (see Appendix F), the measured experimental shift of about 20 nm is reproduced for relative populations of 0.6 in sites ± 3 compared to the population in site 0.

As both M and N increase, the Gaussian SD decreases as expected as the ± 3 sites get cleaned [Fig. 5(e)]. At minimum, the expected SD is 29 nm, which corresponds to the width numerically obtained from Eq. (13). We measured an SD of 45 ± 5 nm, which is slightly larger than the expected one. This expected width limit (square points) corresponds to the case of perfect alignment of the two lattices. It is however very sensitive to the relative angle between the lattice wave vectors. In Appendix G, we compute the effective SD $\tilde{\sigma}_x$ after adding a rotation by an angle η_y about the y axis between the two lattices. We show that in the small-angle limit the SD is given by $\tilde{\sigma}_x = \sigma_x\sqrt{1 + \eta_y^2(\sigma_y/\sigma_x)^2}$. For only 0.3° [star points in Fig. 5(e)], the calculated widths overlap with the experimental data.

IV. CONCLUSION

In this work, we have super-resolved the atomic position using the high sensitivity of atomic properties to a spatially varying electromagnetic environment. In particular, we have demonstrated that excited-state energy shifts were a versatile and well-controlled solution to manipulate atomic transition frequencies over very short distances. We have given a general theoretical framework to describe subwavelength imaging dynamics and derived the expected localization performance for two opposite regimes of imaging strength for which we have determined validity criteria. Both regimes lead to conceptually very different situations, but achieve similar resolution capabilities. Experimentally, in Sec. III B we first applied our excited-state engineering method in the strong imaging regime. Imaging optically resolved slices of atoms, we have demonstrated an excitation length around 100 nm. This resolution is well explained and quantitatively corresponds to a model accounting for the internal state dynamics of a 3LS. We emphasize that the excitation length estimate relies on an absolute measurement of atom numbers. The quantitative match between the model and experimental data for large optical depths (low modulation depths) requires us to account for a nonnegligible reduction of the scattering cross section that was characterized in Ref. [17]. For small excitation lengths, the effect of kinetic energy could be mitigated by deeply entering into the strong imaging regime (shorter time and higher transfer rate). In the nonoptically resolved limit (Sec. III C), we have shown that the resolution could be strongly improved using excited-state energy shifts varying at the scale of the wavelength. These shifts were created using counterpropagating laser fields. Such an experiment was performed in the opposite weak imaging regime. The method was used to image a strongly compressed atomic density of SD 21 nm and we obtained an image of SD 45 ± 5 nm, well below the diffraction limit. The increase is attributed both to the finite resolution and to a possible residual fringe misalignment.

One should note that the proposed subwavelength imaging method mostly addresses the part of the cloud that is finally imaged, leaving the rest of the cloud little perturbed. As such, it can be used to shape and quench the dynamics of the system. Regarding the practical implementation, nonperiodic transfer could be reached using structured light excited-state dressing that would further enable a parallelized and tunable imaging of multiple slices. As compared to Refs. [15,16], the position selectivity of the presented method also depends on the standing wave positions, but can additionally be fine tuned by the adjustment of the repumping radiation frequency. The repumping radiation power directly affects the on-resonant scattering rate that sets the imaging strength and allows us to scan from the weak to the strong imaging regime.

The current experiments and numerical simulations have been performed for ^{87}Rb atoms. However, it can be straightforwardly extended to other alkali metals with large excited-state hyperfine splittings such as cesium atoms. For alkalis with lower excited-state splittings, the method could straightforwardly be extended to the large field limit that only results in a redefinition of the proper eigenbasis. In our imaging system, we used fast absorption imaging to infer atom numbers. Single-atom fluorescence detection [1,28] could be straightforwardly implemented to reach single-atom sensitivity by reading out the hyperfine state $|2\rangle$. With our method, the resolution depends both on the excited-state shift and on the excited-state linewidth, making it favorable for atomic species with narrow transitions. For instance, spectrally resolved imaging has been demonstrated using an ultranarrow optical transition in ytterbium atoms [29]. Other examples of usable narrow optical transitions include strontium and dysprosium species. For such narrow transitions (Γ small), the strong imaging regime criterion ($\mathcal{S} \gg 1$) can hardly be reached as $\mathcal{S} \propto \Gamma^3$, while the weak imaging regime criterion ($\mathcal{W} \ll 1$) is favored as $\mathcal{W} \propto \Gamma^2$, but hardly allows us to image the state with high temporal resolution. We finally emphasize that our method could be spin selective by taking advantage of the differential light shifts between Zeeman states for circularly polarized 1529-nm beams.

ACKNOWLEDGMENTS

R.V. acknowledges PhD support from the University of Bordeaux; J-B.G. and V.M. acknowledge support from the French State, managed by the French National Research Agency (ANR) in the frame of the Investments for the Future Programme IdEx Bordeaux-LAPHIA (ANR-10-IDEX-03-02). This work was also supported by ANR contracts (JCJC ANR-18-CE47-0001-01 and QUANTERA21 ANR-22-QUA2-0003) and the Quantum Matter Bordeaux.

APPENDIXES

In Appendix A, we compare the experimental light shifts induced by the 1529-nm laser to theoretical computations. In Appendix B, we justify the reduction to a three-level system that is used to model the internal state transfer dynamics. In Appendix C, we describe the spatiotemporal dynamics during the transfer, the weak and strong imaging regimes with analytical criteria for their domain of validity, and simulate the full system for the experiments presented in the manuscript. In Appendix D, we discuss the impact of the light-shift gradient of the excited state for the experimental conditions. In Appendix E, we show how the piezo stack controlling the 1064 nm is calibrated. Finally, we simulate the wavepacket microscopy sequence in the 1064-nm lattice to study the influence of experimental imperfections on the central position of the wavepacket in Appendix F and its associated width in Appendix G.

APPENDIX A: LIGHT SHIFT AT 1529 nm

The light shifts induced by the 1529-nm laser are computed by diagonalizing the total Hamiltonian composed of the ac Stark Hamiltonian and the hyperfine Hamiltonian [30].

To compute the light shifts for a far-off-resonance laser, the counter-rotating term of the atom-field interaction has to be included. As both terms oscillate rapidly compared to each other, both light shifts computed independently from each other can be added after their respective diagonalization in their own rotating frame.

The numerical computations of the light shifts of state $5P_{3/2}$ with a laser at exactly 1529.360 98 nm includes the following states: $5S_{1/2}$, $5P_{1/2}$, $5P_{3/2}$, $6P_{1/2}$, $4D_{3/2}$, and $4D_{5/2}$. The main transitions that contribute to the light shifts are $5P_{3/2}$ to $4D_{5/2}$ at 1529.366 nm with a dipole moment of $10.899ea_0$, and $5P_{3/2}$ to $4D_{3/2}$ at 1529.262 nm with a dipole moment of $3.628ea_0$, where e is the electron charge and a_0 is the Bohr radius. Typical atomic parameters for ^{87}Rb can be found in Refs. [31,32]. Our 1529-nm laser mainly drives the transition between $5P_{3/2}$ and $4D_{5/2}$, as depicted in Fig. 1(a). The theoretical light shift is ultimately obtained by knowledge of the intensity of the 1529-nm laser beams which are uniform over the cloud widths. Individual waists of 131 and 138 μm are measured using a tomography technique [33]. The intensity is controlled by the locked optical power and yields, for instance, a peak intensity of 4.1×10^5 W/m^2 for an optical power per beam of 2.9 mW. The 1529-nm resonance is found by a spectroscopic scan onto the atoms.

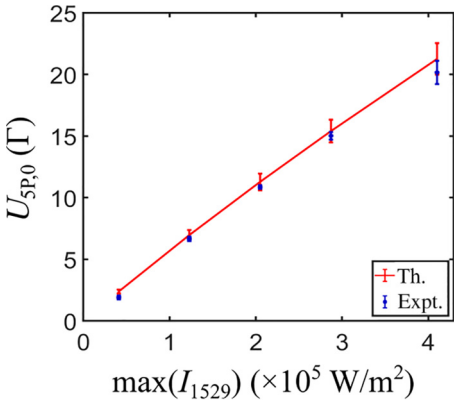

FIG. 6. Experimental light shifts obtained from tomographic measurements compared to the theoretical shifts computed from knowledge of the waists, frequency, and powers of the 1529-nm beams. Error bars correspond to the waist uncertainty for the theoretical model and to the standard deviation over five realizations for the experimental data.

We compared this theoretical description of the light shift with the experimental realizations in Fig. 6 for the homogeneous cloud configuration. Five repetitions of a tomographic curve are measured, from which the light shifts are obtained by fitting the atom number with Eq. (C3c). Both agree, which enables us to precisely compute the spatial resolution with Eq. (10) where the light shift is an input parameter.

APPENDIX B: THREE-LEVEL SYSTEM REPUMP MODEL FOR ^{87}Rb

Figure 7 shows the effective 3LS that we consider to model the point spread function based on the multilevel structure of ^{87}Rb.

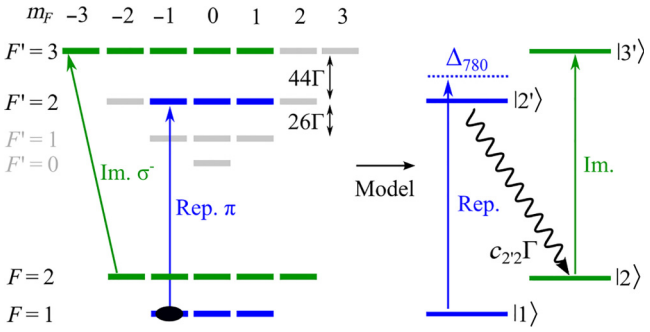

FIG. 7. ^{87}Rb D_2 transition hyperfine structure ($5^2S_{1/2}$ to $5^2P_{3/2}$) and its approximation as a 3LS for the repumper transition and as a 2LS for the imaging transition.

The differential light shifts between the m_F states of $F' = 2$ for a π-polarized 1529-nm laser are much lower than the atomic linewidth $\Gamma/2\pi = 6.066$ MHz. As a result, there is no dark state in the hyperfine ground state $F = 1$ as all m_F states can be locally coupled to the excited state. We numerically checked that taking all the states coupled by π transitions or approximating it as a two-level system leads to the same population transfer. Therefore, we treat the multilevel repumper transition as the two-level system: $|1\rangle$ and $|2'\rangle$ (blue levels in Fig. 7). For this two-level system, as the atom is initially prepared in $|5^2S_{1/2}, F = 1, m_F = -1\rangle$, we include in the saturation parameter the coupling strength of the transition between $|5^2S_{1/2}, F = 1, m_F = -1\rangle$ and $|5^2P_{3/2}, F' = 2, m_F = -1\rangle$ of $-\sqrt{1/8}$ [34], which leads to a saturation intensity of $I_{\mathrm{sat,rep}} = 6.67\ \mathrm{mW/cm^2}$.

We ignore the coupling from $|1\rangle$ to the excited state $|5^2P_{3/2}, F' = 1, m_F = -1\rangle$ as it is 26Γ away from $|2'\rangle$, which is smaller than the 1529-nm induced light shifts of the experiment.

The population in $|1\rangle$ is transferred via absorption and spontaneous emission cycles into $F = 2$ and remains there: we treat all m_F states of $F = 2$ as a single state $|2\rangle$.

Finally, the population in $|2\rangle$ is measured by absorption imaging using a circularly polarized laser tuned on the cycling transition from $|5^2S_{1/2}, F = 2, m_F = -2\rangle$ to $|5^2P_{3/2}, F' = 3, m_F = -3\rangle$.

APPENDIX C: SPATIOTEMPORAL DYNAMICS DURING IMAGING

1. Temporal dynamics

The point spread function, defined in our system as the spatially dependent population transfer rate to $|2\rangle$ [$\kappa(x)$], is derived from the time evolution of the density matrix ρ of the 3LS in the absence of spatial dynamics [30].

We focus on slow dynamics ($\Gamma t \gg 1$) by applying the adiabatic approximation that assumes that the optical coherences are always in equilibrium with respect to the populations ($\dot{\rho}_{12'} \approx 0$). This regime is valid for thermal atoms if their displacement over a time $1/\Gamma$ is much smaller than the target subwavelength resolution. Atoms at 169 nK (Sec. III B) move by 170 pm during the 28 ns of the scattering event, which is indeed much smaller than the target resolution of 10 nm. In this case, the 3LS density matrix evolution simplifies to the rate equations

$$\frac{d}{dt}\begin{pmatrix}\rho_{11}\\ \rho_{2'2'}\\ \rho_{22}\end{pmatrix} = \begin{pmatrix}-s\Gamma/2 & s\Gamma/2 + c_{2'1}\Gamma & 0\\ s\Gamma/2 & -s\Gamma/2 - \Gamma & 0\\ 0 & c_{2'2}\Gamma & 0\end{pmatrix}\begin{pmatrix}\rho_{11}\\ \rho_{2'2'}\\ \rho_{22}\end{pmatrix}, \tag{C1}$$

where $c_{2'1} = 1/2$ (respectively $c_{2'2} = 1/2$) is the normalized decay rate from $|2'\rangle$ to $|1\rangle$ (respectively $|2\rangle$) due to spontaneous emission at rate Γ, and $s(x) = s_0/\{1 + [2\Delta(x)/\Gamma]^2\}$.

An analytical solution of Eq. (C1) is obtained by the diagonalization method. Starting from the initial state $\rho_{11}(t = 0) = 1$, for any saturation parameter, the populations are equal to

$$\rho_{11} = 1 - \rho_{2'2'} - \rho_{22}, \tag{C2a}$$

$$\rho_{2'2'} = \frac{\Gamma + \Lambda_- + \Lambda_+}{2(\Lambda_- - \Lambda_+)}(e^{\Lambda_+ t} - e^{\Lambda_- t}), \tag{C2b}$$

$$\rho_{22} = 1 - \frac{\Lambda_-}{\Lambda_- - \Lambda_+}e^{\Lambda_+ t} + \frac{\Lambda_+}{\Lambda_- - \Lambda_+}e^{\Lambda_- t}, \tag{C2c}$$

where $\Lambda_\pm = -\Gamma/2(1 + s \pm \sqrt{1 + 2sc_{2'1} + s^2})$ correspond to nonzero eigenvalues.

The $e^{\Lambda_+ t}$ terms decay to zero at a rate of Γ so the long time dynamics is mainly given by the $e^{\Lambda_- t}$ terms. The solutions in the low-saturation limit $s_0 \ll 1$ and for $\Gamma t \gg 1$ simplify to

$$\rho_{11}(x) \approx 1 - \rho_{22}(x), \tag{C3a}$$

$$\rho_{2'2'}(x) \approx \frac{1}{2}\frac{s_0}{1 + [2\Delta(x)/\Gamma]^2} \times \exp\left\{-\frac{c_{2'2}\Gamma t}{2}\frac{s_0}{1 + [2\Delta(x)/\Gamma]^2}\right\}, \tag{C3b}$$

$$\rho_{22}(x) \approx 1 - \exp\left\{-\frac{c_{2'2}\Gamma t}{2}\frac{s_0}{1 + [2\Delta(x)/\Gamma]^2}\right\}. \tag{C3c}$$

The population in $|2\rangle$ can be reinterpreted as a depumping from $|1\rangle$ with rate

$$\kappa(x) = \frac{c_{2'2}s_0\Gamma}{2}\frac{1}{1 + [2\Delta(x)/\Gamma]^2} = \frac{\kappa_0}{1 + (x/X_0)^2}, \tag{C4}$$

where $\kappa_0 = c_{2'2}s_0\Gamma/2$ is the on-resonance transfer rate and $X_0 = i_{1529}\Gamma/(2\pi U_{5\mathrm{P},0})$ is the characteristic subwavelength length scale that was obtained by linearizing $\Delta(x) = U_{5\mathrm{P},0}/2\Gamma \sin(k_{1529}x)$ around $x = 0$ (midfringe).

It is interesting to mention that FWHMs can be derived for any resonance condition starting from the expression of $\rho_{22}(x)$. For instance, when the repumper laser is tuned at the bottom of the modulation where $\Delta_{780} = 0$, the FWHM in the strong imaging regime is

$$\mathrm{FWHM_s^{bottom}} = \left(\frac{2\Gamma}{U_{5\mathrm{P},0}}\right)^{1/2}\frac{i_{1529}}{\pi}\left(\frac{c_{2'2}\Gamma s_0 t}{2\ln(2)}\right)^{1/4}. \tag{C5}$$

This configuration is relevant for probing the site occupancy rather that the intrasite details.

2. Spatiotemporal dynamics

The strong localization of particles induced by the imaging process translates to rapid spatial variation of the

density profile. It corresponds to a high kinetic energy term that influences the imaging dynamics itself. To phenomenologically account for this effect, we model the depumping from state $|1\rangle$ by a non-Hermitian loss term in the Schrödinger equation:

$$i\hbar\frac{d\,|\Psi(x,t)\rangle}{dt} = \hat{H}_0\,|\Psi(x,t)\rangle - i\frac{\hbar\kappa(\hat{x})}{2}\,|\Psi(x,t)\rangle\,. \quad \text{(C6)}$$

Here $\hat{H}_0$ is the Hamiltonian including kinetic and potential energies of a harmonic oscillator with eigenstates $|n\rangle$ and eigenvalues E_n such that $\hat{H}_0\,|n\rangle = E_n\,|n\rangle$ with $|n\rangle$ corresponding to the harmonic oscillator wave function given by $\Phi_n(x) = \langle x|n\rangle$. In Eq. (C6), we have neglected the interactions between particles. Indeed, in the first experiment, the atoms are in a shallow trap that ensures weak interactions. In the second experiment, a 1D regime applies along the deep lattice direction. Equation (C6) is valid for both the strong and weak imaging regimes. A numerical integration is possible for any set of experimental parameters.

In the following subsections, we present the simulations carried out for the experimental situations encountered in the main text. To gain in generality, we also algebraically derive the criteria that correspond to the weak and strong imaging limits.

3. Strong imaging criteria

In the strong imaging regime, we imprint a dip in $\Psi(x,t)$. This generates a velocity spread Δv. In that case, one should satisfy $\Delta v.t_{\text{imaging}} \ll \Delta x$, where Δx is the position spread.

In the main text, we discussed the simple and analytical case of a Gaussian dip that satisfies the Heisenberg equality. The opposite limit is represented by the steep gate function of width L for which the velocity spread is infinite. To better model the real probability distribution [Eqs. (C3)] whose velocity spread is not analytic, we approximate ρ_{22} by a C^1 analytic solution ($\rho_{22}^{\text{approx}}$) with conserved amplitude and slope at half width at half maximum compared to Eq. (C3c):

$$\rho_{22}^{\text{approx}} = \frac{A}{2}\begin{cases} 1+\sin[\alpha(x+x_0)], & |x+x_0| < \pi/2\alpha, \\ 2, & |x| < x_0 - \pi/2\alpha, \\ 1+\sin[\alpha(x-x_0)], & |x-x_0| < \pi/2\alpha, \\ 0, & \text{otherwise}, \end{cases} \quad \text{(C7)}$$

with $A = (1-\exp\{-\kappa_0 t\})/\text{FWHM} \approx 1/\text{FWHM}$ in the deep depletion limit ensuring that $\int \rho_{22}(x)dx = 1$, $x_0 = \text{FWHM}/2$, and $\alpha = 4\ln 2^{3/2}/X_0\sqrt{\kappa_0 t}$.

The kinetic energy of a particle of mass m in wave function $\Psi_{22} = \sqrt{\rho_{22}^{\text{approx}}(x)}$ can be defined as

$$E_c = \frac{m\Delta v^2}{2} = \frac{\hbar^2}{2m}\int \Psi_{22}^{\text{approx}}(x)\Delta\Psi_{22}^{\text{approx}}(x)dx = \frac{\alpha}{8\text{FWHM}}. \quad \text{(C8)}$$

Therefore, a Lorentzian pumping scheme leads to the velocity spread expression

$$\Delta v = \frac{\hbar\sqrt{\ln 2}}{m\text{FWHM}}. \quad \text{(C9)}$$

Equation (C9) is used to compute the condition on the pumping strength given by Eq. (8) in the main text.

4. Weak imaging criteria

The Schrödinger equation (C6) has an adiabatic evolution with respect to the motional states of the harmonic oscillator if the coupling strength satisfies

$$|\,\langle\phi_n|\,\kappa(\hat{x})\,|\phi_0\rangle\,| \ll \frac{2(E_n - E_0)}{\hbar}, \quad \text{(C10)}$$

where the factor of 2 on the right-hand side comes from the dissipation term $\kappa(\hat{x})/2$ in the Schrödinger equation.

It can be explicitly evaluated using the harmonic oscillator eigenfunctions given by the Hermite polynomials H_n:

$$\langle x|\phi_n\rangle = \sqrt{\frac{1}{2^n n!}}\left(\frac{1}{\pi {a_{\text{HO}}}^2}\right)^{1/4} e^{-x^2/2a_{\text{HO}}^2} H_n\left(\frac{x}{a_{\text{HO}}}\right) \quad \text{(C11)}$$

with a_{HO} the harmonic oscillator width.

Using the expression of the dissipation $\kappa(\hat{x})$, we get

$$\langle\phi_n|\,\kappa(\hat{x})\,|\phi_0\rangle = \frac{\kappa_0}{\sqrt{\pi 2^n n!}}\int_{-\infty}^{+\infty}\frac{dx}{a_0}\,\frac{H_n(x/a_0)e^{-x^2/a_0^2}H_0(x/a_0)}{1+(x/X_0)^2}. \quad \text{(C12)}$$

After a change of variable $x = a_{\text{HO}}X$, and using $H_0(X) = 1$, it simplifies as

$$\langle\phi_n|\,\kappa(\hat{x})\,|\phi_0\rangle = \frac{\kappa_0}{\sqrt{\pi 2^n n!}}\int_{-\infty}^{+\infty} dX\,\frac{H_n(X)e^{-X^2}}{1+(X/r_0)^2}, \quad \text{(C13)}$$

where $r_0 = X_0/a_{\text{HO}}$.

So far, this criterion corresponds to the case where the dissipation operator is centered with respect to the harmonic oscillator. Including a position offset x_r for the

dissipation, the matrix element is written more generally as

$$\langle\phi_n|\,\kappa(\hat{x}-x_r)\,|\phi_0\rangle = \frac{\kappa_0}{\sqrt{\pi 2^n n!}}\int_{-\infty}^{+\infty} dX \frac{H_n(X)e^{-X^2}}{1+(X/r_0 - x_r/X_0)^2}. \tag{C14}$$

Equation (C14) gives the matrix element without approximation for any position x_r. In the following, we evaluate it in the strong localization limit ($r_0 \ll 1$) to derive simple analytical criteria for the adiabaticity, and give a resolution for the case $x_r = 0$ beyond this limit.

Strong localization limit. From Eq. (C14), in the limit of strong localization where $r_0 \ll 1$, we can treat the Lorentzian function as a Dirac distribution, i.e.,

$$\lim_{r_0\to 0}\frac{1}{1+[X/r_0 - x_r/X_0]^2} = \pi r_0 \delta\left(X - \frac{x_r}{a_{\mathrm{HO}}}\right), \tag{C15}$$

which yields

$$\langle\phi_n|\,\kappa(\hat{x}-x_r)\,|\phi_0\rangle = \kappa_0 r_0\sqrt{\frac{\pi}{2^n n!}}H_n\left(\frac{x_r}{a_{\mathrm{HO}}}\right)e^{-(x_r/a_{\mathrm{HO}})^2}. \tag{C16}$$

Maximizing this matrix element with respect to the repumping position x_r is equivalent to finding the smallest root x_n of H_{n+1}, as it can be shown using Hermite polynomial recursion relations for $H_n'(x)$. For even $n \geq 2$, the matrix element is maximum at $x_n = 0$, while for odd $n \geq 1$, it is maximum at the first antinode of H_n. There is unfortunately no formula for the positions of those roots for any n, so we found them algebraically for $n = 1, 2$ for which $x_1 = 1/\sqrt{2}$ and $x_2 = 0$. We also verified numerically that $\mathcal{W}_n = \langle\phi_n|\,\kappa(\hat{x}-x_r)\,|\phi_0\rangle/n$ is monotonically decreasing with n and that the adiabatic condition is fulfilled in the strong localization limit:

$$\mathcal{W}_1 = \sqrt{\pi}e^{-1/2}\frac{\kappa_0 r_0}{2\omega_{\mathrm{HO}}} + o(r_0) \ll 1, \tag{C17a}$$

$$\mathcal{W}_2 = \sqrt{\frac{\pi}{8}}\frac{\kappa_0 r_0}{2\omega_{\mathrm{HO}}} < \mathcal{W}_1, \tag{C17b}$$

$$\mathcal{W}_{n+1} < \mathcal{W}_n \quad \text{for all } n. \tag{C17c}$$

Beyond the strong localization limit. Beyond the strong localization limit, it is possible to get analytical results for the matrix element in the case $x_r = 0$.

For odd n, the Hermite polynomials are odd, so $\langle\phi_n|\,\kappa(\hat{x})\,|\phi_0\rangle = 0$. It is due to the fact that the dissipation is centered about the harmonic oscillator center. Therefore, an odd state cannot be coupled from an even state. Odd states could be coupled in the case where there would be a spatial offset between the dissipation and the harmonic oscillator.

For even n, $\langle\phi_n|\,\kappa(\hat{x})\,|\phi_0\rangle$ is nonzero and can be computed using the general polynomial expansion of the Hermite functions:

$$H_n(X) = n!\sum_{m=0}^{\lfloor n/2\rfloor}\frac{(-1)^m}{m!\,(n-2m)!}(2X)^{n-2m} \tag{C18}$$

with $\lfloor\cdot\rfloor$ denoting the floor function.

Using Eq. (C18), the coupling term $\langle\phi_n|\,\kappa(\hat{x})\,|\phi_0\rangle$ for even n reads

$$\langle\phi_n|\,\kappa(\hat{x})\,|\phi_0\rangle = \frac{\kappa_0 r_0^2 e^{-r_0^2}}{\sqrt{\pi 2^n}}\sqrt{n!}\sum_{m=0}^{n/2}(-1)^m\frac{2^{n-2m}}{m!\,(n-2m)!} \times \Gamma_f\left[\tfrac{1}{2}(1-2m+n)\right]\mathrm{Ei}_{(1-2m+n)/2}(r_0^2), \tag{C19}$$

where Γ_f is the gamma function and Ei is the generalized exponential integral function.

From this result, we can extract an exact analytical expression for the adiabaticity criterion for any even quantum number n. The most stringent adiabatic criterion given by Eq. (C10) is obtained for $n = 2$:

$$\left|\frac{\kappa_0 r_0^2 e^{r_0^2}}{2\sqrt{2}}[\mathrm{Ei}_{1/2}(r_0^2) - \mathrm{Ei}_{3/2}(r_0^2)]\right| \ll 2\omega_{\mathrm{HO}}. \tag{C20}$$

Equivalently, Eq. (C20) can be written as

$$\left|\frac{\kappa_0 r_0}{2\sqrt{2}}[2r_0 - (1+2r_0^2)e^{r_0^2}\sqrt{\pi}\,\mathrm{erfc}(r_0)]\right| \ll 2\omega_{\mathrm{HO}}, \tag{C21}$$

where erfc is the complementary error function.

In the regime of strong localization of the wave function where $r_0 \ll 1$, the criterion leads to $\mathcal{W}_2$ in Eq. (C17b).

5. Numerical simulation of the evolution

The diabatic and adiabatic behavior of the wave function respectively expected in the strong and weak imaging regimes can be validated by numerical simulations of Eq. (C6). For that purpose, using the imaginary time method, we have derived the ground and few first eigenstate wave functions of $\hat{H}_0$. Starting from the ground state, we suddenly apply at time $t = 0$ the loss term in Eq. (C6) and numerically simulate the temporal evolution until t_{tr} at which the loss term is removed and the system measured. The results of such a simulation are presented in Fig. 8 for the experimental parameters [s_0, t_{tr} (μs)] corresponding to the data of the main text.

For the strong imaging regime [Fig. 8(a)], the initial state is a Gaussian state with size $\sigma_y = 64$ μm. The solid line is the simulation carried out for parameters (0.022, 8)

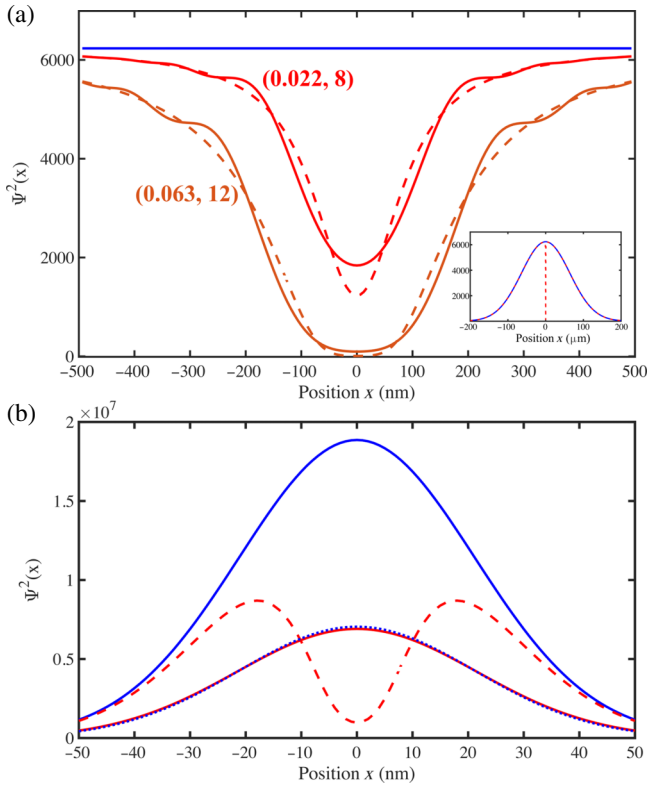

FIG. 8. Simulation of the evolution of the wave function. The solid blue lines correspond to the initial wave function. The other solid curves correspond to the simulation of Eq. (C6) and the dashed curves are the strong imaging limit of Eq. (9). (a) Simulation in the strong coupling regime corresponding to the experimental parameters in Sec. III B, ($s_0 = 0.022$, $t_{tr} = 8$ μs) and ($s_0 = 0.063$, $t_{tr} = 12$ μs), which are respectively shown in red and orange. Inset: full view of the wave function. (b) Simulation in the weak coupling regime corresponding to the experimental parameters in Sec. III C, ($s_0 = 0.02$, $t_{tr} = 16$ μs), $\omega = 2\pi \cdot 130$ rad kHz. The dotted line corresponds to the equilibrium solution derived from Eq. (13). To highlight the difference between the two regimes, we show the wave function (red dashed line) if the strong imaging limit applies.

and (0.063, 12), which is slightly smoothed by the evolution, but still very close to the strong imaging limit (dashed line) calculated from Eq. (9). The inset shows the entire wave function with the repumped region show with a red dashed line.

For the weak imaging regime [Fig. 8(b)], we start from the ground state of a 130-kHz harmonic oscillator frequency and repump with (0.02,12). The resulting simulated wave function (red solid line) strongly differs from the strong imaging limit (red dashed line). On the other hand, it corresponds very well to the adiabatic evolution (dotted blue line) that is calculated from Eq. (13), and corresponds to a reduction of the initial wave function (solid blue line).

APPENDIX D: FORCES DURING EXCITATION

The imaging method involves the use of strong light-shift gradients, possibly corresponding to non-negligible dipole forces during the time the atoms transit in the excited state. It might have two effects: a distortion of the ground-state potential via a doubly dressed state (DDS) effect, and a strong acceleration of the atoms before being imaged by absorption imaging.

We compute the doubly dressed state potential corresponding to the average force that includes the ground- and excited-state potentials [7]:

$$U_{\mathrm{DDS}}(x) = \int_{-\infty}^{x} dy \left[\rho_{5\mathrm{S}}(\Delta) \frac{dU_{5\mathrm{S}}}{dy} + \rho_{5\mathrm{P}}(\Delta) \frac{dU_{5\mathrm{P}}}{dy} \right]. \tag{D1}$$

Using $\rho_{5\mathrm{P}} + \rho_{5\mathrm{S}} = 1$ and the detuning $\Delta = \Delta_{780} - (U_{5\mathrm{P}} - U_{5\mathrm{S}})$, Eq. (D1) becomes

$$U_{\mathrm{DDS}}(x) = \int_{-\infty}^{x} dy \left[\frac{dU_{5\mathrm{S}}}{dy} - \rho_{5\mathrm{P}}(\Delta) \frac{d\Delta}{dy} \right]. \tag{D2}$$

Performing the integration with $\rho_{5\mathrm{P}}(Y) = (s_0/2)/(1 + s_0 + Y^2)$ and setting the limits $U_{5\mathrm{S}}(-\infty) = U_{5\mathrm{P}}(-\infty) = 0$, the doubly dressed state potential simplifies to

$$\begin{aligned} U_{\mathrm{DDS}}(x) &= U_{5\mathrm{S}}(x) - \int_{2\Delta(-\infty)/\Gamma}^{2\Delta(x)/\Gamma} dY \rho_{5\mathrm{P}}(Y) \\ &= U_{5\mathrm{S}}(x) - \frac{s_0 \Gamma}{4\sqrt{1+s_0}} \\ &\quad \times \left[\mathrm{atan}\left(\frac{2\Delta(x)}{\Gamma\sqrt{1+s_0}} \right) - \mathrm{atan}\left(\frac{2\Delta_{780}}{\Gamma\sqrt{1+s_0}} \right) \right]. \end{aligned} \tag{D3}$$

We apply Eq. (D3) for our case at the midfringe ($\Delta_{780} = U_{5\mathrm{P},0}/2$), aligned on a ground-state lattice site, with a linearized detuning, and use $s_0 \ll 1$ to obtain

$$U_{\mathrm{DDS}}(x) = U_{5\mathrm{S}}(x) - \frac{s_0 \Gamma}{4} \left[\mathrm{atan}\left(\frac{x}{X_0} \right) - \mathrm{atan}\left(\frac{U_{5\mathrm{P},0}}{\Gamma} \right) \right]. \tag{D4}$$

The total Hamiltonian in the Schrödinger equation now includes the potential given by Eq. (D4) and the kinetic energy such that $\hat{H}_{\mathrm{tot}} = \hbar U_{\mathrm{DDS}}(\hat{x}) + \hat{H}_{\mathrm{kinetic}}$. From this total Hamiltonian, we can extract an adiabaticity criterion where the effect of the strong light shifts does not excite motional states:

$$|\langle \phi_n | \hat{H}_{\mathrm{tot}} | \phi_0 \rangle| \ll E_n - E_0 = n\hbar\omega_{\mathrm{HO}}. \tag{D5}$$

The sum of the 5*S* potential and the kinetic energy is diagonal in the state basis. Therefore, only the atan term in the

potential creates off-diagonal couplings. As the excited-state potential is odd, only odd couplings are nonzero and, for $n = 1$, reads

$$\sqrt{\frac{\pi}{8}}\frac{\kappa_0}{c_{2'2}\omega_{\mathrm{HO}}}e^{r_0^2}\mathrm{erfc}(r_0) \ll 1. \tag{D6}$$

In the strong localization limit ($r_0 \ll 1$), the term $e^{r_0^2}\mathrm{erfc}(r_0) \approx 1$. Therefore, it does not depend on the light-shift amplitude, but only on the interaction strength set by κ_0. It is expected as s_0 determines the trap depth due to the excited state in the doubly dressed state potential [Eq. (D4)]. In our experimental settings where $r_0 = 0.24$, it reads $0.23 \ll 1$, which guarantees that the ground-state potential is weakly perturbed by the strong light shift of the excited state. It is interesting to note that the effect of the strong gradient could in principle be neglected using a repumper laser resonant with the bottom of the excited-state lattice where the derivative is zero.

Finally, let us estimate the impact of the acceleration on the atom number measurements after the transfer into $|2\rangle$ due to the force of the excited state. The force at the mid-fringe is equal to $F_0 = \pi U_{5\mathrm{P},0}/i_{1529}$. The atom velocity can be computed using the equation of motion $m\dot{v} = F_0$. After an average time in the excited state of the order of $1/\Gamma$, the atoms transferred into $|2\rangle$ have on average a velocity gain of $v = \pi U_{5\mathrm{P},0}/(mi_{1529}\Gamma)$. For an absorption imaging time $t_{\mathrm{im}} = 8$ μs, the atoms moved by 0.088 μm (respectively 0.4 μm) in experiments with the thermal cloud (respectively the BEC), which is smaller than the size of a pixel (0.8 μm) at the position of the atoms. Therefore, the absorption imaging is not impacted by this acceleration as the displacement of the atoms is smaller than the pixel size. Even for larger displacements, reliable atom number measurements can be done if the signal to noise per pixel is higher than 1, and if the Doppler effect along the imaging beam propagation direction is negligible (the acceleration due to the light shifts is in the transverse place).

APPENDIX E: PIEZO DISPLACEMENT CALIBRATION

The piezo stack controlling the position of the 1064-nm lattice is calibrated by measuring the displacement of the atomic fringes on a camera as a function of the piezo drive, as shown in Fig. 9. These fringes are obtained after loading the 1064-nm lattice and turning *on* the 1529-nm lattice. The atoms are repumped with $\Delta_{780} = 0\Gamma$ and imaged by absorption imaging. The piezo displacement axis is ultimately calibrated by knowing that two consecutive fringes along the site number axis are equal to $13i_{1064} = 6.9$ μm. Along the piezo displacement axis, a displacement of exactly i_{1064} gives the same fringe position due to the lattice periodicity. Note that the fringe visible around site $n^\circ 0$ at a displacement of $0.6i_{1064}$ corresponds to site $n^\circ - 1$, which is resonant.

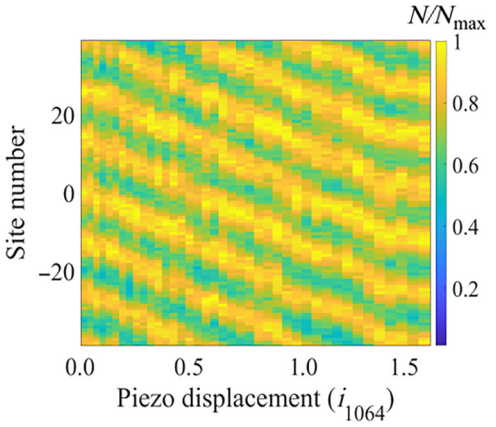

FIG. 9. Projection along the x axis of normalized atom numbers after repumping atoms in the 1064-nm lattice with $\Delta_{780} = 0$, $s_0 = 0.02$, and $t = 8$ μs in a modulation of $U_{5\mathrm{P},0} = 16\Gamma$ as a function of the camera axis (y axis) and the relative phase Φ_0 (x axis) between the two lattices.

APPENDIX F: CENTRAL POSITION SHIFTS

We numerically compute the position shift of the imaged wavepacket by simulating the total repumped fraction for different relative populations in sites ±3 compared to the population in site 0. We numerically scan the relative phase between the lattices knowing the initial atomic density and the point spread function $\rho_{22}(x)$ from which we compute the repumped populations. Then, we fit the resulting wavepacket with a Gaussian function to extract the central position. We see in Fig. 10 that, for populations of approximately 0.6, the wavepacket shifts by ±20 nm, which corresponds to the experimental data. We checked that residual angles as described in Appendix G do not significantly shift the position of the wavepacket.

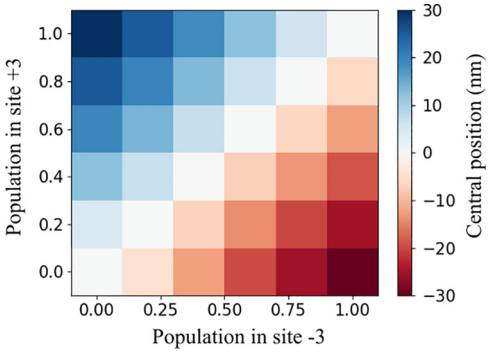

FIG. 10. Central position shift of the wavepacket as a function of the relative initial populations in sites ±3.

APPENDIX G: WIDTH BROADENING BY LATTICE MISALIGNMENT

The atomic density in the ground-state lattice site is characterized by the widths $\sigma_x \ll \sigma_{y,z}$ and $\sigma_y = \sigma_z$. Let us consider a 2D Gaussian atomic density in a rotated frame (x', i') by an angle η_i such that

$$n(x', i') = \exp\left\{-\frac{x'^2}{2\sigma_x^2} - \frac{i'^2}{2\sigma_i^2}\right\}. \tag{G1}$$

The rotated frame is expressed in the initial frame by

$$\begin{pmatrix} x' \\ i' \end{pmatrix} = \begin{pmatrix} \cos(\eta_i) & -\sin(\eta_i) \\ \sin(\eta_i) & \cos(\eta_i) \end{pmatrix} \begin{pmatrix} x \\ i \end{pmatrix}, \tag{G2}$$

where $i \in \{y, z\}$.

Integrating Eq. (G1) over direction i, using $\sigma_y \gg \sigma_x$ and considering the case of small angles $\eta_i \ll 1$, one can compute the linear atomic density

$$n(x) = e^{-x^2/2\tilde{\sigma}_x^2}, \tag{G3}$$

where the effective width $\tilde{\sigma}_x$ is given in the main text.

It is clear that a rotation about the x axis does not lead to any broadening as the potential is symmetric.

In the case of a relative angle η_z about the z axis (Fig. 11), the projection of the repumped cloud along y is shifted on the order of σ_y, which corresponds to an angle of 0.3°. Experimentally, the cloud shifts by less than a micrometer, so we believe that η_z does not contribute to a broadening. Note that other datasets showed shifts of the order of a few micrometers. We could minimize these shifts by a better alignment of the counterpropagating 1529-nm laser beam.

The angle η_y is difficult to estimate experimentally. On the one hand, the z direction is integrated by the imaging system, so we do not have access to that spatial direction to look for a displacement of the projection. On the other hand, a small displacement of the order of σ_x is difficult to measure along x.

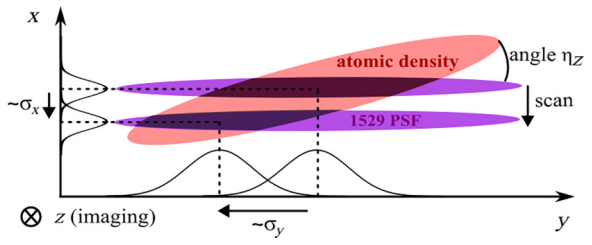

FIG. 11. Schematics of the projection position shift of the repumped atomic cloud in the case of a relative angle η_z between an atomic wavepacket and a 1529-nm point spread function plane.

As in Appendix F, we performed a complete simulation of the measured wavepacket, but we also included η_y as a free parameter. We use the initial population in the ±3 sites that we found in Appendix F. For this population and using $\eta_y = 0.3°$, we numerically compute a width of 69 nm after the coarse cleaning step, which matches with the experimental data of Fig. 5(e) in the main text. Also, we found that the expected width after the second cleaning step matches with the experimental width of 45 ± 5 nm. The effect of an angle is to globally shift the theoretical line towards larger widths.

Other sources of broadening could be considered in the case of perfect alignment. We ensured that the lattice laser frequencies do not drift significantly by frequency locking them on the same transfer cavity. Then, the initial phase at the atom position might also fluctuate over time due to room-temperature changes. This would lead to an imperfect initial positioning of site 0 at the beginning of the first cleaning sequence. It would cause an asymmetry in the measured wavepacket in the second cleaning step as either the −3 site or +3 site would be closer or further from resonance. Finally, the last repumper pulse can be shortened to durations smaller than the trap frequency period to avoid dynamical effects. We tried to use shorter repumper durations and did not see a narrower wavepacket, which suggests that the dominating width broadening was due to a residual angle, as in such a case the dynamics in the trap along x would be on longer timescales than along x'.

[1] F. Schäfer, T. Fukuhara, S. Sugawa, Y. Takasu, and Y. Takahashi, Tools for quantum simulation with ultracold atoms in optical lattices, Nat. Rev. Phys. **2**, 411 (2020).

[2] A. Mazurenko, C. S. Chiu, G. Ji, M. F. Parsons, M. Kanász-Nagy, R. Schmidt, F. Grusdt, E. Demler, D. Greif, and M. Greiner, A cold-atom Fermi-Hubbard antiferromagnet, Nature **545**, 462 (2017).

[3] J. Koepsell, S. Hirthe, D. Bourgund, P. Sompet, J. Vijayan, G. Salomon, C. Gross, and I. Bloch, Robust bilayer charge pumping for spin- and density-resolved quantum gas microscopy, Phys. Rev. Lett. **125**, 010403 (2020).

[4] S. Nascimbene, N. Goldman, N. R. Cooper, and J. Dalibard, Dynamic optical lattices of subwavelength spacing for ultracold atoms, Phys. Rev. Lett. **115**, 140401 (2015).

[5] T.-C. Tsui, Y. Wang, S. Subhankar, J. V. Porto, and S. L. Rolston, Realization of a stroboscopic optical lattice for cold atoms with subwavelength spacing, Phys. Rev. A **101**, 041603(R) (2020).

[6] R. P. Anderson, D. Trypogeorgos, A. Valdés-Curiel, Q.-Y. Liang, J. Tao, M. Zhao, T. Andrijauskas, G. Juzeliunas, and I. B. Spielman, Realization of a deeply subwavelength adiabatic optical lattice, Phys. Rev. Res. **2**, 013149 (2020).

[7] M. Bellouvet, C. Busquet, J. Zhang, P. Lalanne, P. Bouyer, and S. Bernon, Doubly dressed states for near-field trapping and subwavelength lattice structuring, Phys. Rev. A **98**, 023429 (2018).

[8] A. G. Godin, B. Lounis, and L. Cognet, Super-resolution microscopy approaches for live cell imaging, Biophys. J. **107**, 1777 (2014).
[9] M. G. L. Gustafsson, Surpassing the lateral resolution limit by a factor of two using structured illumination microscopy, J. Microsc. **198**, 82 (2000).
[10] S. W. Hell and J. Wichmann, Breaking the diffraction resolution limit by stimulated emission: Stimulated-emission-depletion fluorescence microscopy, Opt. Lett. **19**, 780 (1994).
[11] M. J. Rust, M. Bates, and X. Zhuang, Sub-diffraction-limit imaging by stochastic optical reconstruction microscopy (STORM), Nat. Methods **3**, 793 (2006).
[12] C. Weitenberg, M. Endres, J. F. Sherson, M. Cheneau, P. Schauß, T. Fukuhara, I. Bloch, and S. Kuhr, Single-spin addressing in an atomic Mott insulator, Nature **471**, 319 (2011).
[13] A. Alberti, C. Robens, W. Alt, S. Brakhane, M. Karski, R. Reimann, A. Widera, and D. Meschede, Super-resolution microscopy of single atoms in optical lattices, New J. Phys. **18**, 053010 (2016).
[14] L. Asteria, H. P. Zahn, M. N. Kosch, K. Sengstock, and C. Weitenberg, Quantum gas magnifier for sub-lattice-resolved imaging of 3D quantum systems, Nature **599**, 571 (2021).
[15] M. McDonald, J. Trisnadi, K.-X. Yao, and C. Chin, Super-resolution microscopy of cold atoms in an optical lattice, Phys. Rev. X **9**, 021001 (2019).
[16] S. Subhankar, Y. Wang, T.-C. Tsui, S. L. Rolston, and J. V. Porto, Nanoscale atomic density microscopy, Phys. Rev. X **9**, 021002 (2019).
[17] R. Veyron, V. Mancois, J.-B. Gerent, G. Baclet, P. Bouyer, and S. Bernon, Quantitative absorption imaging: The role of incoherent multiple scattering in the saturating regime, Phys. Rev. Res. **4**, 033033 (2022).
[18] J. Keeling and N. G. Berloff, Spontaneous rotating vortex lattices in a pumped decaying condensate, Phys. Rev. Lett. **100**, 250401 (2008).
[19] I. G. Savenko, T. C. H. Liew, and I. A. Shelykh, Stochastic Gross-Pitaevskii equation for the dynamical thermalization of Bose-Einstein condensates, Phys. Rev. Lett. **110**, 127402 (2013).
[20] J. Sierra, A. Kasimov, P. Markowich, and R.-M. Weishäupl, On the Gross–Pitaevskii equation with pumping and decay: Stationary states and their stability, J. Nonlinear Sci. **25**, 709 (2015).
[21] M. Ben Dahan, E. Peik, J. Reichel, Y. Castin, and C. Salomon, Bloch oscillations of atoms in an optical potential, Phys. Rev. Lett. **76**, 4508 (1996).
[22] E. Whiting, An empirical approximation to the Voigt profile, J. Quant. Spectrosc. Radiat. Transf. **8**, 1379 (1968).
[23] Y.-J. Lin, A. R. Perry, R. L. Compton, I. B. Spielman, and J. V. Porto, Rapid production of ^{87}Rb Bose-Einstein condensates in a combined magnetic and optical potential, Phys. Rev. A **79**, 063631 (2009).
[24] X. Li, F. Zhou, M. Ke, P. Xu, X.-D. He, J. Wang, and M.-S. Zhan, High-resolution ex vacuo objective for cold atom experiments, Appl. Opt. **57**, 7584 (2018).
[25] R. Veyron, V. Mancois, J. B. Gerent, G. Baclet, P. Bouyer, and S. Bernon, Effective two-level approximation of a multilevel system driven by coherent and incoherent fields, Phys. Rev. A **105**, 043105 (2022).
[26] B. Gadway, D. Pertot, R. Reimann, M. G. Cohen, and D. Schneble, Analysis of Kapitza-Dirac diffraction patterns beyond the Raman-Nath regime, Opt. Express **17**, 19173 (2009).
[27] J. H. Denschlag, J. E. Simsarian, H. Häffner, C. McKenzie, A. Browaeys, D. Cho, K. Helmerson, S. L. Rolston, and W. D. Phillips, A Bose-Einstein condensate in an optical lattice, J. Phys. B: At. Mol. Opt. Phys. **35**, 3095 (2002).
[28] A. Fuhrmanek, R. Bourgain, Y. R. P. Sortais, and A. Browaeys, Free-space lossless state detection of a single trapped atom, Phys. Rev. Lett. **106**, 133003 (2011).
[29] K. Shibata, R. Yamamoto, Y. Seki, and Y. Takahashi, Optical spectral imaging of a single layer of a quantum gas with an ultranarrow optical transition, Phys. Rev. A **89**, 031601(R) (2014).
[30] D. A. Steck, Quantum and atom optics (2019), available online at http://steck.us/teaching, revision 0.12.6.
[31] B. Arora and B. K. Sahoo, State-insensitive trapping of Rb atoms: Linearly versus circularly polarized light, Phys. Rev. A **99**, 049901(E) (2019).
[32] B. Arora, M. S. Safronova, and C. W. Clark, Magic wavelengths for the np-ns transitions in alkali-metal atoms, Phys. Rev. A **76**, 052509 (2007).
[33] A. Bertoldi, S. Bernon, T. Vanderbruggen, A. Landragin, and P. Bouyer, In situ characterization of an optical cavity using atomic light shift, Opt. Lett. **35**, 3769 (2010).
[34] D. A. Steck, Rubidium 87 D line data (2001), available online at http://steck.us/alkalidata.